

Assessing the applicability of a smeared crack approach for simulating the behaviour of concrete beams flexurally reinforced with GFRP bars and failing in shear

Joaquim A.O. Barros^{a,*}, Hadi Baghi^b, A. Ventura-Gouveia^c

^a ISISE, Institute of Science and Innovation for Bio-Sustainability (IB-S), Department of Civil Engineering, University of Minho, 4800-058 Guimarães, Portugal

^b Design Engineer at Structural Design Inc., Ann Arbor, MI, USA

^c ISISE, Department of Civil Engineering, Polytechnic Institute of Viseu, 3504-510 Viseu, Portugal

ARTICLE INFO

Keywords:

Smeared crack approach
Beams failing in shear
GFRP flexural reinforcement
Crack shear stress transfer

ABSTRACT

Numerical simulation of beams failing in shear is still a challenge. With the scope of verifying the applicability of smeared crack approaches to simulate the behavior of reinforced concrete (RC) beams failing in shear, a set of concrete beams reinforced with longitudinal glass fiber reinforced polymer (GFRP) bars, experimentally tested up to their failure, and comprehensively monitored, are numerically simulated. The simulations are carried out with a multi-directional fixed smeared crack model available in the FEMIX computer program that has several options for modeling the crack shear stress transfer, which is a critical aspect when simulating RC elements failing in shear. The predictive performance of the numerical simulations is assessed in term of load vs deflection, crack pattern at failure, concrete strains in critical shear regions, and moment–curvature relationship. The influence on the predictive performance of the following modeling aspects is also investigated: finite element mesh refinement; simulation of the crack shear stress transfer by using the classical shear retention factor and a crack shear-softening diagram; bond conditions between flexural reinforcement and surrounding concrete. The simulations carried out demonstrate that small dependence of the results on the finite element mesh refinement and adequate crack patterns can be obtained with refinement levels suitable for design purposes and taking into account the actual computer performances, as long as a crack shear-softening diagram is used. However, the predictive performance of the simulations depends significantly on the values adopted for the parameters that define this diagram, as demonstrated by the performed parametric studies.

1. Introduction

Glass fiber reinforced polymer (GFRP) bars have been increasingly used as flexural reinforcement in concrete beams and slabs due, mainly, to their immunity to corrosion, high strength-to-weight ratio, and non-magnetic nature [1–6]. However, when compared to steel bars applied in the reinforcement of concrete structures, GFRP bars have smaller elasticity modulus (E_f), bond performance and fatigue resistance [7–9], their mechanical properties are more detrimentally affected by high temperature (above their glass transition temperature, which is relatively small), [10–12], have more brittle behaviour (linear-elastic up to abrupt tensile rupture), and are more difficult of being deformed for ensuring proper anchorage conditions. The smaller E_f and less efficient bond behaviour to concrete of some type of GFRP bars, as flexural

reinforcement, place extra challenges in terms of accomplishing the design requisites for serviceability limit state conditions, mainly in terms of crack width and deflection of concrete members flexurally reinforced with this type of bars [3,13].

In the context of the shear capacity of reinforced concrete (RC) elements, the use of GFRP bars as flexural reinforcement can have detrimental implications in terms of dowel effect and aggregate interlock, since their smaller axial and shear stiffness allows the occurrence of larger opening and sliding of the critical diagonal cracks.

Considerable research has been dedicated to assess the effect of the longitudinal (flexural) FRP reinforcement ratio (ρ_f) and its stiffness on the shear strength of RC elements. While Yost et al. [14], indicated that the GFRP longitudinal reinforcement ratio did not affect the shear capacity, Al-Khrdaji et al. [15], El-Sayed et al. [16,17], Matta et al. [18],

* Corresponding author.

E-mail addresses: barros@civil.uminho.pt (J.A.O. Barros), ventura@estgv.ipv.pt (A. Ventura-Gouveia).

Tureyen and Frosch [19], and Razaqpur et al. [20], demonstrated that the shear strength of concrete beams flexurally reinforced with GFRP and CFRP bars was proportional to the ρ_l .

The influence of concrete compressive strength, shear span to cross section's depth ratio (a/d_f , see Fig. 1), ρ_l , and axial stiffness of the longitudinal reinforcement ($\rho_l E_l$) on the failure mechanisms and beam's shear capacity has been investigated [21]. In general, the influence of concrete compressive strength, a/d_f and ρ_l on the beam's shear strength follow the same tendency verified in beams flexurally reinforced with steel bars. Regarding the $\rho_l E_l$, it was verified that the beam's shear strength increases with the $\rho_l E_l$ [22].

For predicting the behaviour of RC beams for serviceability and ultimate limit state conditions, material nonlinear analysis based on the finite element method (FEM) are the most powerful approaches, since, the load-deformation response, the strain and stress fields in the constituent materials, the type of failure mode and crack pattern can be assessed, but the level of assessment accuracy depends on the type of constitutive model adopted.

Numerical tools for brittle fracture simulation are usually based on continuous smeared (SCM) or discontinuous discrete crack (DCM) models. In SCM, fracture is modelled on average sense, by smearing the effect of cracks into a continuum solid via stress-strain relations. However, dependence of the results on the adopted finite element mesh refinement has been reported [23], which leads to deep concerns on using SCM on design practice, mainly in structures presenting brittle failure modes, such is the type of RC beams considered in the present work. DCM have the virtue of simulating more closely the physical separation of a crack, and several variants of DCM have been proposed, namely, by using interface finite elements (IFE) [24], partition-of-unity (POU) based methods [25], embedded strong discontinuities (ESD) [26–28], and lattice models (LM) [29].

However, in the IFE the crack paths are constrained to propagating along element edges, by requiring very refined FE meshes for capturing realistic crack patterns, unless this approach is used to simulate the behaviour of RC structures where the critical cracks are already formed, such is the case of modeling crack-damaged RC structures in the context of their strengthening [30]. In the POU and some ESD approaches, the computational cost is generally too high due to the complex procedures to enrich the finite elements and/or nodes. In the LM, the computational cost is also very high due to the large number of finite elements that this type of approaches requires, together with the difficulties on assessing the values for the material properties of their model parameters.

Due these limitations of the IFE, POU and ESD approaches, the SCM are still the most implemented in the FEM-based commercial software, so they are the most used by structural designers.

For RC elements failing in bending, SCM have demonstrated to be capable of predicting with good accuracy the main behavioural aspects if the relevant properties of the intervenient materials are appropriately provided, namely the constitutive law that defines the concrete fracture mode I propagation, the yield stress of the flexural reinforcement and their bond conditions with the surrounding concrete. However, crack width and stress field in the reinforcements at serviceability limit state conditions are still difficult of estimating, due to the continuous nature of SCM.

The essential nonlinear modelling concepts for the analysis and design RC structures, the fundamentals of the most current FEM-based approaches, and the strategies the user of these approaches should adopt to minimize potential errors and inaccurate simulations are treated elsewhere [31].

A recent blind competition on the simulation of RC beams failing in shear by using FEM-based approaches [32] has demonstrated the challenges the design community face for estimating the load-deflection, failure mode, crack pattern and strain level in critical regions of this type of beams. Despite the provided experimental data for the definition of the relevant models' parameters, inaccuracies on the load capacity, deflection and strain at peak load have attained 40%, 113% and 600%, respectively.

For RC beams failing in shear, the methodology adopted for simulating the crack shear stress transfer when using SCM has a significant impact on the predictive performance of these type of approaches.

In the context of SCM, the crack shear stress transfer is generally simulated by using a shear retention factor that can be a constant value [33,34], decrease with the increase of the crack opening according to a certain evolution law [35,36], or even considering, besides the crack opening, the crack sliding and the maximum aggregate size [37], and also approaches that still consider the influence of the reinforcement in the cracking zone [38], due to its crack width restrain effect and consequent impact on the favorable aggregate interlock shear resisting mechanism. However, all these possibilities of simulating the crack shear stress transfer conduct to overestimations of the failure load [39–41]. Another alternative for modeling the crack shear stress transfer is the adoption of a crack shear softening diagram [42], since good predictive performance in RC beams failing in shear [41] and RC slabs failing in punching [43] has been reported. However, the evaluation of

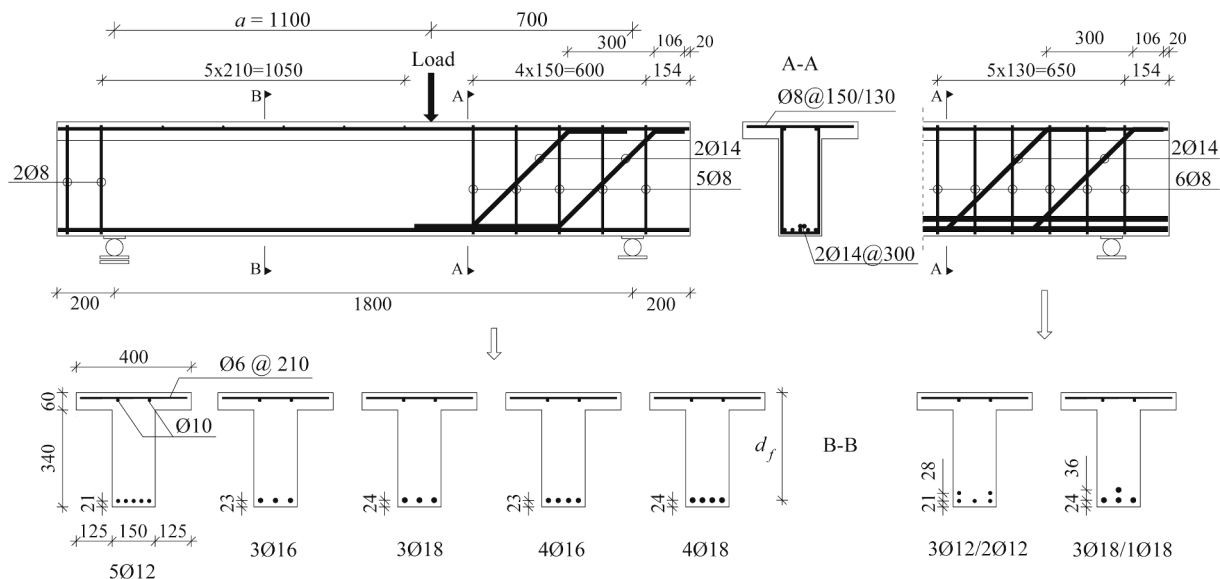


Fig. 1. Geometry, reinforcement details, and support and loading conditions of the beams of the test program (dimensions in mm) (adapted from [22]).

the values for the parameters that define this diagram still requires reliable experimental test methodologies, and/or design recommendations.

The concept of shear retention, evaluated as constant or depending on the crack opening, as well as crack shear softening diagram for modeling the crack shear stress transfer are available in the multidirectional fixed smeared crack model (MDFSCM) of the FEMIX computer program [44]. The potentialities and debilities of the MDFSCM for modeling the behaviour of RC beams failing in shear are appraised in this work. For this purpose, it was selected a set of RC beams failed in shear, without shear reinforcement in the failure span length, and flexurally reinforced with GFRP bars. These attributes introduce extra challenges on the numerical simulations due to the linear-elastic behaviour of GFRP up to its abrupt tensile rupture, specific bond conditions of this type of reinforcement, and lower elasticity modulus than of conventional steel reinforcements, which can affect detrimentally the aggregate interlock and dowel shear resisting mechanisms.

For performing these studies, a comprehensive experimental program was selected [22], where the relevant properties of the constituent materials are provided, an extensive monitoring was adopted for measuring the deformability, curvature and bending moment in critical sections, as well as axial and distortional strains and crack patterns.

The analysis includes the assessment of the influence of the finite element mesh refinement on the relevant results, influence of using the shear retention factor versus crack shear softening diagram, and bond conditions between the GFRP flexural reinforcement and surrounding concrete. Finally, parametric studies are conducted to assess the influence of the parameters defining the crack shear softening diagram on the predictive performance of the numerical simulations.

2. Experimental program

2.1. Introduction

The experimental program carried out by Kaszubska et al. [22] was selected for appraising the performance of the MDFSCM in predicting the behaviour of RC beams failing in shear. In this section only relevant information of this experimental program for the numerical simulations is provided, but the details can be found in the previously indicated reference and in Kaszubska [21].

2.2. Materials, specimens, test setup, monitoring system and relevant results

The experimental program was composed by the seven T cross section beams, whose geometry, reinforcement arrangements, support and

loading conditions are shown in Fig. 1. All beams have two GFRP bars of 10 mm diameter as compressive longitudinal reinforcement localized in the flange, which are supported on transversal short steel bars of 6 mm diameter spaced at 210 mm for ensuring the aimed position of these GFRP bars in the cross section. In the larger shear span (herein designated by testing zone) no stirrups are provided, while the shorter shear span was reinforced with closed steel stirrups of 8 mm diameter at 130/150 mm spacing, and steel bent bars of 14 mm diameter, in order to force the occurrence of shear failure in the testing zone.

Fig. 2 shows the monitoring system applied in each experimentally tested beam. It is formed by eight displacement transducers (LVDT) mounted on an independent steel frame for measuring the vertical deflection of the beam (LVDTs 22 to 29), four LVDTs for recording the concrete compressive strains in the flange (LVDTs 1 to 4), and four LVDTs for measuring the concrete tensile strains in the web at the level of the flexural reinforcement (LVDTs 5 to 8). For evaluating the shear deformations in the testing zone, four sets of LVDTs were disposed in a triangle configuration (delta rosettes) with a LVDT per each edge of the triangle (LVDTs 9 to 21).

The load was applied under displacement control at 10 $\mu\text{m/s}$ by using a T cross section steel profile to distribute the load along the width of the flange (contacted area of 10 mm \times 400 mm).

The average tensile strength (f_{fu}) and average modulus of elasticity (E_l) of the GFRP bars adopted for the flexural reinforcement (12, 16 and 18 mm diameter) were determined by executing tensile tests according to [45], and the obtained results are indicated in Table 1.

From compression tests executed according to [46] recommendations with 16 concrete cylinders of 150 mm diameter and 300 mm height, an average compressive strength (f_{cm}) of 30.1 MPa (COV = 8%) was obtained, while splitting tensile tests according to Brazilian test setup have provided an indirect tensile strength ($f_{ct,sp}$) of 2.9 MPa (COV = 8%).

To identify the beams of the experimental program, the X ϕ Y acronym was adopted, where X is the number of bars of ϕ Y diameter (in mm). For instance, 5 ϕ 12 is a beam flexurally reinforced with a layer of 5

Table 1

Tensile strength and longitudinal modulus of elasticity of GFRP bars used for the flexural reinforcement of the tested beams.

Type of bars	Nominal bar diameter [mm]	f_{fu} [MPa]	E_l [GPa]
GFRP	12	1195 (6; 4.7%)	50.2 (5; 0.4%)
	16	1089 (3; 1.4%)	50.5 (3; 0.4%)
	18	987 (6; 9.8%)	50.9 (5; 2.4%)

The values in round brackets indicate the number of tested specimens and the coefficient of variation.

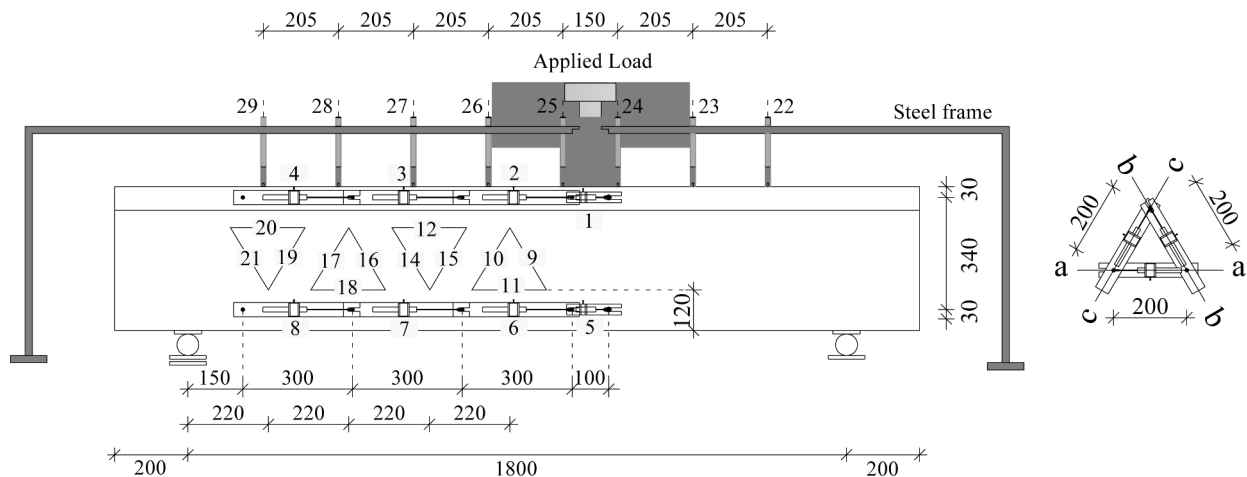


Fig. 2. Monitoring system (dimensions in mm) (adapted from [22]).

bars of 12 mm diameter. In the beams with two layers of flexural reinforcement, the beam's identification is $X_1\phi Y_1/X_2\phi Y_2$, where X_i and ϕY_i represent the number and diameter of the i^{th} layer (1 or 2, being the 1st layer closest to the bottom tensile surface of the beam). The cover thickness of the most external layer of the flexural reinforcement was 15 mm. The relevant characteristics of the beams of this experimental program, and the main results from the testes carried out are indicated in Table 2. In this table: NL is the number of layers of the tensile flexural reinforcement (1 or 2); A_l and $\rho_l = A_l/(b d_{l,eq})$ are the cross sectional area and the reinforcing ratio of the tensile flexural reinforcement, where b and $d_{l,eq} = \sum_{i=1}^{NL} (A_i d_i) / \sum_{i=1}^{NL} (A_i)$ are the width of the web's cross section and the equivalent internal arm of the flexural reinforcement ($d_{l,eq} = d_1$ when the flexural reinforcement is composed by only one layer); $V_{max} = 7/18 F_{max}$ is the maximum shear force in the test zone at the beam's maximum load (F_{max}); and $\delta_{F_{max}}$ is the deflection at the loaded section at F_{max} .

The results show a tendency for the increase of the shear capacity with ρ_l and ϕ_l , mainly when the flexural reinforcement is formed by two layers, which reflects the favorable mechanism of the dowel effect for the beam's shear capacity. This favorable mechanism has contributed for the tendency of the tested beams in presenting smaller deflection at failure as larger is ρ_l and ϕ_l , but the interval of $\delta_{F_{max}}$ values was relatively narrow (from 2.7 up to 5.2 mm).

3. Numerical simulations

3.1. Introduction

In this chapter is described the modeling strategies for a critical assessment of the potentialities of the MDFSCM in the prediction of the behaviour of RC beams failing in shear, namely the ones tested experimentally, described in the previous section. This assessment covers several fundamental aspects like: influence of finite element mesh refinement on the beam's load–deflection performance and crack pattern at failure (Section 3.3); capacity of predicting the moment–curvature and concrete strains (Section 3.4); influence of the bond conditions for modeling the interface between flexural reinforcement and surrounding concrete on the beam's load carrying capacity, deformation performance, and crack pattern at failure (Section 3.5); influence on the predictive performance of the simulations when using a shear softening diagram versus shear retention factor for modeling the crack shear stress transfer (Section 3.6). Since it will be demonstrated the relevance of using a crack shear softening diagram for modeling the crack shear stress transference, a parametric study is carried out to show the influence of each parameter of this constitutive model on the relevant beam's behavioural aspects (Section 3.7).

The following section is dedicated to a brief description of the constitutive models for simulating the behaviour of the intervenient materials.

3.2. Constitutive models of the intervenient materials

3.2.1. Concrete

In the present simulations, the 2D version of the MDFSCM described

in detail elsewhere [39,40] was used. Thereby, in the present section only the fundamental aspects are highlighted for a comprehensive analysis of model's capabilities on the simulations of RC beams failing in shear. At a generic integration point (IP) of a finite element, the relationship between the incremental strain and stress vectors, $\Delta \underline{\sigma} = \underline{D}^{crco} \Delta \underline{\epsilon}$, is established from the following constitutive equation [39,40]:

$$\Delta \underline{\sigma} = \left(\underline{D}^{co} - \underline{D}^{co} [\underline{T}^{cr}]^T \left(\underline{D}^{cr} + \underline{T}^{cr} \underline{D}^{co} [\underline{T}^{cr}]^T \right)^{-1} \underline{T}^{cr} \underline{D}^{co} \right) \Delta \underline{\epsilon} \quad (1)$$

where \underline{D}^{co} is the elasticity matrix according to Hooke's law (dependent on the Young's modulus and Poisson's coefficient of the concrete, E_c and ν_c). Since in beams failing in shear by the formation of critical diagonal cracks, the maximum compressive stress is relatively low, the concrete in compression is assumed developing linear and elastic behaviour, but the possibility of simulating the nonlinear behaviour in compression is also available in FEMIX computer program [39,47].

In Eq. (1) $\underline{T}^{cr}(\theta^{cr})$ is the transformation matrix between crack strain components in the coordinate system of the crack, $\Delta \underline{\epsilon}_1^{cr}$ (two components per crack, normal $\Delta \epsilon_n^{cr}$, and shear $\Delta \gamma_t^{cr}$, where n and t define the coordinate system of the crack), and crack strain components in the global coordinate system of the structure, $\Delta \underline{\epsilon}^{cr}$ (three components per IP), i.e.,

$$\Delta \underline{\epsilon}^{cr} = \left[\underline{T}^{cr}(\theta^{cr}) \right]^T \Delta \underline{\epsilon}_1^{cr}. \text{ The } \underline{T}^{cr}(\theta^{cr}) \text{ depends on the angle between the}$$

abscissa axis of the global coordinate system of the structure and the orthogonal to the crack plane (axis n). Since more than one crack can be formed in each IP, according to the criterion adopted for crack initiation, the dimension of $\underline{T}^{cr}(\theta^{cr})$ and $\Delta \underline{\epsilon}_1^{cr}$ varies with the number of active cracks, n_{cr} ($[n_{cr} \times 2] \times 3$ for the $\underline{T}^{cr}(\theta^{cr})$ and $[n_{cr} \times 2] \times 1$ for the $\Delta \underline{\epsilon}_1^{cr}$). In Eq. (1), \underline{D}^{cr} is the crack constitutive matrix defining the fracture mode I (D_n^{cr}) and fracture mode II (D_t^{cr}) moduli. The dimension of \underline{D}^{cr} also depends on the number of active cracks ($[n_{cr} \times 2] \times [n_{cr} \times 2]$). For simulating the fracture mode I propagation, the trilinear diagram represented in Fig. 3a was adopted, which depends on the stress at crack initiation, $\sigma_{n,1}^{cr} = f_{ct}$, the α_i and ξ_i parameters that define the shape of the diagram, the mode I fracture energy, $G_{F,I}$, and the crack bandwidth, l_b , that aims to ensure results not dependent on the finite element mesh refinement. In all the simulations carried out in the present work, the l_b was assumed equal to the square root of the area of the IP.

For modeling the shear stress transfer between both faces of a crack, the $\tau_t^{cr} - \gamma_t^{cr}$ diagram represented in Fig. 4 was adopted, where the initial shear fracture modulus, $D_{t,1}^{cr}$, is defined by:

$$D_{t,1}^{cr} = \frac{\beta}{1 - \beta} G_c \quad (2)$$

being G_c the concrete elastic shear modulus, and β the shear retention factor defined as a constant value in the range]0,1[.

The ultimate crack shear strain, $\gamma_{t,u}^{cr}$ (Fig. 4), depends on the crack shear strength, $\tau_{t,p}^{cr}$, the mode II fracture energy, $G_{F,II}$, and on the crack bandwidth, l_b , as follows:

$$\gamma_{t,u}^{cr} = \frac{2G_{F,II}}{\tau_{t,p}^{cr} l_b} \quad (3)$$

Table 2

Relevant characteristics of the beams of the test program and main results.

Beam's designation	NL	$A_l(\text{mm}^2)$	$\rho_l(\%)$	$d_{l,eq}(\text{mm})$	$\rho_l E_l(\text{GPa})$	$f_{cm}(\text{MPa})$	$f_{ct,sp}(\text{MPa})$	$V_{max}(\text{kN})$	$\delta_{F_{max}}(\text{mm})$
5 ϕ 12	1	565	0.99	379	0.51	30.2	2.75	34.3	5.2
3 ϕ 16	1	603	1.07	377	0.55	28.8	2.95	31.7	3.4
3 ϕ 18	1	763	1.35	376	0.70	28.8	2.95	38.6	2.9
4 ϕ 16	1	804	1.42	377	0.73	30.5	2.70	34.8	2.7
4 ϕ 18	1	1018	1.80	376	0.93	28.8	2.95	38.2	3.0
3 ϕ 12/2 ϕ 12	2	565	1.02	368	0.53	31.7	3.05	34.8	3.7
3 ϕ 18/1 ϕ 18	2	1018	1.85	367	0.95	31.7	3.05	47.7	3.5

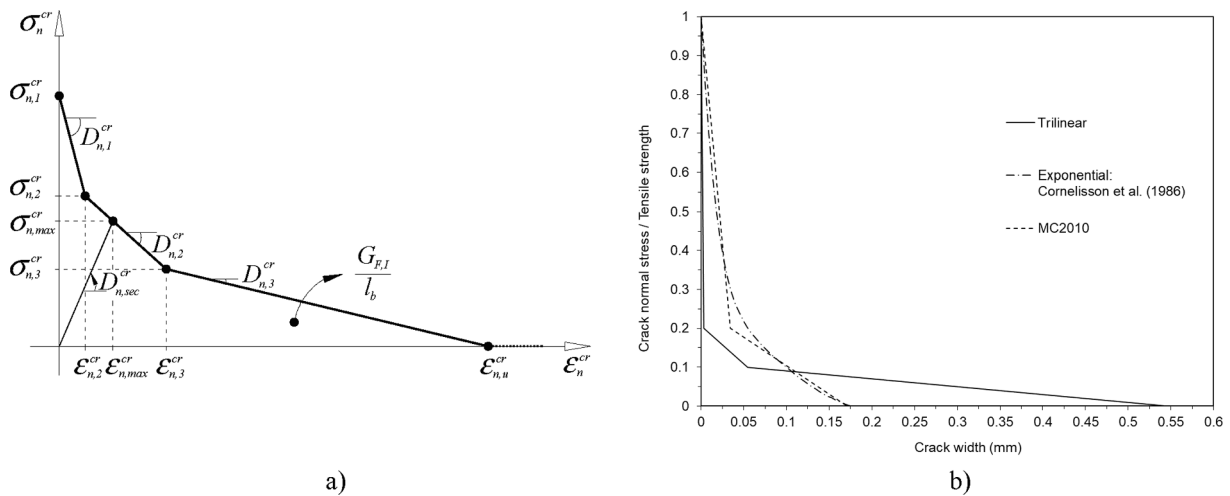


Fig. 3. (a) Trilinear stress-strain diagram to simulate the fracture mode I crack propagation ($\sigma_{n,1}^{cr} = f_{ct}$, $\sigma_{n,2}^{cr} = \alpha_1 \sigma_{n,1}^{cr}$, $\sigma_{n,3}^{cr} = \alpha_2 \sigma_{n,1}^{cr}$, $\epsilon_{n,2}^{cr} = \xi_1 \epsilon_{n,u}^{cr}$, $\epsilon_{n,3}^{cr} = \xi_2 \epsilon_{n,u}^{cr}$), and (b) Normalized stress (divided by the tensile strength) vs crack width relationship used numerically and proposed by MC2010 and Cornelissen et al. [48].

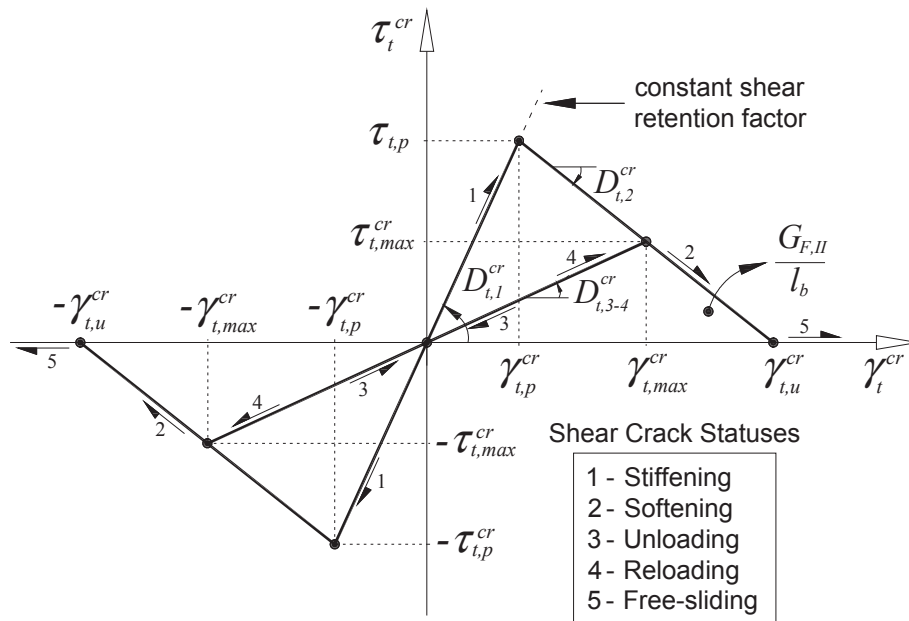


Fig. 4. Diagram to simulate the relationship between the crack shear stress and crack shear strain component, and possible shear crack statuses.

In the present approach, it is assumed that the crack bandwidth, used in an attempt of obtaining results not dependent on the finite element mesh refinement, is the same for both fracture mode I and mode II processes.

3.2.2. Reinforcements

Since the maximum strain level in the beams failed in shear never exceeded the yield strain of the steel, the behaviour of these reinforcements was assumed linear-elastic.

A linear-elastic stress-strain relationship up to a brittle tensile failure was considered for the GFRP bars applied as tensile flexural reinforcement.

3.2.3. GFRP-concrete bond

For the simulations where debond between GFRP bars and surrounding concrete was considered, the following bond stress vs slip law, $\tau - \delta$, was adopted:

$$\tau(\delta) = \begin{cases} \frac{\tau_0}{\delta_0} \delta & \text{if } 0 \leq \delta \leq \delta_0 (4a) \\ \tau_m \left(\frac{\delta}{\delta_m} \right)^{\beta_1} & \text{if } \delta_0 \leq \delta \leq \delta_m (4b) \\ \tau_m \left(\frac{\delta}{\delta_m} \right)^{-\beta_2} & \text{if } \delta > \delta_m (4c) \end{cases}$$

where τ_m and δ_m are the bond strength and its corresponding slip, being β_1 and β_2 the parameters that define the shape of the pre- and post-peak curves. Up to δ_0 is assumed a linear elastic branch (Fig. 5) for the $\tau - \delta$, being the corresponding τ_0 obtained by replacing in Eq. (4b) δ by δ_0 .

3.2.4. Values of the parameters of the constitutive laws of the intervenient materials

The values obtained in the experimental tests with the GFRP bars, presented in Table 1, were considered for modelling their linear-elastic tensile behaviour. For the steel reinforcement was adopted the elasticity

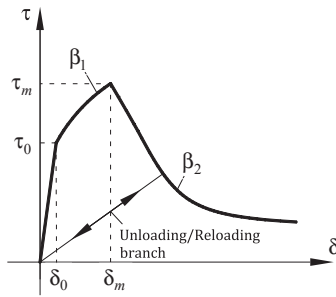


Fig. 5. Bond shear stress-slip law for the slide component of the constitutive law of the interface finite elements.

modulus of 180 GPa obtained elsewhere [21].

The values adopted for the parameters of the concrete constitutive model are those presented in Table 3. Based on the average concrete compressive strength obtained experimentally (30.1 MPa), the Young's modulus, tensile strength and fracture energy were initially determined from the CEB [49], (MC2010) recommendations. By performing preliminary simulations of the tested beams in order to fit as much as possible the initial branch of their force–deflection response up to crack initiation, small modifications have resulted for these values (no more than 10%), which was expectable taking into account the different volume of concrete specimens vs beams and their casting conditions. Since the mode I fracture energy depends on the concrete strength class, water-cement ratio, maximum aggregate size, material type of the aggregates (lightweight vs natural), concrete's age and its curing conditions, the best approach for determining this parameter and the shape of the tensile softening diagram is the execution of direct tensile tests. However, this approach is too time consuming and costly, not applicable at design practice. The bilinear stress-crack width proposed by MC2010 can also be used, which is a simplification of the exponential law obtained by Cornelissen et al. [48]. Another alternative is the derivation of this information by performing inverse analysis with results obtained from notched beam bending tests executed according to the recommendations of RILEM 50-FMC [50]. Since these experimental tests were not executed, the shape of the tensile softening diagram (the α_i and ξ_i parameters) was determined by performing preliminary simulations by fitting as much as possible the force–deflection stage corresponding to cracking propagation. Fig. 3b represents the normalized stress (divided by the tensile strength) vs crack width used numerically (trilinear) and this relationship proposed by MC2010 and Cornelissen et al. [48]. It should be noted that the software transforms the crack width in a crack normal strain by dividing the crack width by the crack bandwidth, which was considered equal to the square root of the finite element.

Table 3

Values of the parameters of the concrete constitutive model.

Property	One row of longitudinal reinforcement	Two rows of longitudinal reinforcement
Poisson's ratio (ν_c)	0.19	
Initial Young's modulus (E_c)	30650 N/mm ²	
Compressive strength (f_c)	30.1 N/mm ²	
Trilinear tension-softening diagram	$f_{ct} = 2.2$ N/mm ² ; $G_{F,I} = 0.075$ N/mm $\xi_1 = 0.006$; $\alpha_1 = 0.2$; $\xi_2 = 0.1$; $\alpha_2 = 0.1$	
Parameter defining the mode I fracture energy available for the new crack	$p_2 = 3$	
Parameters for defining the softening crack shear stress-shear strain diagram	$\tau_{tp}^c = 1.0$ N/mm ² ; $G_{F,II} = 0.05$ N/mm $\beta = 0.4$	$\tau_{tp}^c = 1.1$ N/mm ² ; $G_{F,II} = 0.045$ N/mm $\beta = 0.2$
Crack bandwidth, l_b	Square root of the area of the element	
Threshold angle	$\alpha_{th} = 30^\circ$	
Maximum number of cracks per integration point	2	

Based on these diagrams it is verified that, up to a crack width of approximately 0.1 mm, the MC2010 and Cornelissen et al. [48], approaches propose a higher post-cracking tensile capacity than the one used in the numerical simulations, being the opposed after this crack width. The ultimate crack width obtained with the relationship used in the numerical simulations is almost three times higher than the one determined from the MC2010 and Cornelissen et al. [48]. In these preliminary simulations, the data for defining the crack shear softening diagram was also determined. The experience of the authors accumulated in previous simulations of RC elements failing in shear has also contributed for a relatively fast process of the tailoring process of the values of these parameters [41,51].

A maximum number of two cracks per IP was assumed, and a new crack (2nd in this specific case) was formed in an IP when the principal tensile stress has attained the concrete tensile strength and the angle formed by this principal tensile stress and the orientation of the already existing crack (defined by the orthogonal to the crack plane) is ≥ 30 degrees (threshold angle, α_{th}). For the mode I fracture energy to be attributed to the new crack ($G_{F,I}^{next}$) in a certain IP, the approach proposed in Barros [52], was adopted:

$$G_{F,I}^{next} = (G_{F,I} - G_{F,I,a}) \left(\frac{\alpha}{\pi/2} \right)^{p_2} + G_{F,I,a} \quad (5a)$$

where:

$$G_{F,I,a} = G_{F,I} - G_{F,I,c}^{prev} \quad (5b)$$

is the available mode I fracture energy of the previous crack, obtained by subtracting the fracture energy consumed by the previous crack, $G_{F,I,c}^{prev}$, from the concrete fracture energy, $G_{F,I}$. In Eq. (5a) α is the angle (in radians) between the new and the previous closest crack (≥ 30 degrees, as indicated previously), and p_2 is a parameter that, in the present analysis, was considered equal to 3.

3.3. – Influence of the refinement of the finite element mesh

To investigate the influence of the refinement of the finite element mesh on the relevant results of the tested beams, three levels of refinement were adopted, by considering finite elements of 10×10 mm², 20×20 mm² and 40×30 mm² (width \times depth) dimension. The resulting finite element meshes are presented in Fig. 6, which correspond to the 5 ϕ 12 beam, but the differences for the other beams are restricted to those of two layers of flexural reinforcement, due to the finite elements adopted for simulating the second layer of flexural reinforcement. The finite element meshes are composed of Lagrangian 4-nodes finite elements with 2×2 Gauss-Legendre integration scheme (G-Le_IS) for the concrete, and embedded cable type elements with 2 IP according to the G-Le_IS for the steel reinforcements (in all simulations) and for the GFRP bars when assumed in perfect bond conditions. For simulating perfect bond conditions, embedded cable type finite element was used. The axial strain in each integration point of this element is obtained from the displacements registered in the nodes of the corresponding “mother element”, e.g. the finite element simulating the concrete crossed by the embedded cable. In the analysis considering the possibility of occurring slip between the GFRP and the concrete (simulations made in section 3.5), interface finite elements (IFE) are disposed between the GFRP bars and surrounding concrete. In this case, the GFRP bars were simulated by 2D frame type elements with geometric and mechanical characteristics equal to those considered for the embedded cable type finite elements. An IFE is formed by the nodes of the frame type finite element representing the GFRP and the nodes of the finite element simulating the concrete the GFRP bar is touching. In these simulations, IFE of 4 nodes with 2 IP according to the Gauss-Lobato integration scheme (G-Lo_IS) were used.

Fig. 7 compares the load vs deflection in the loaded section,

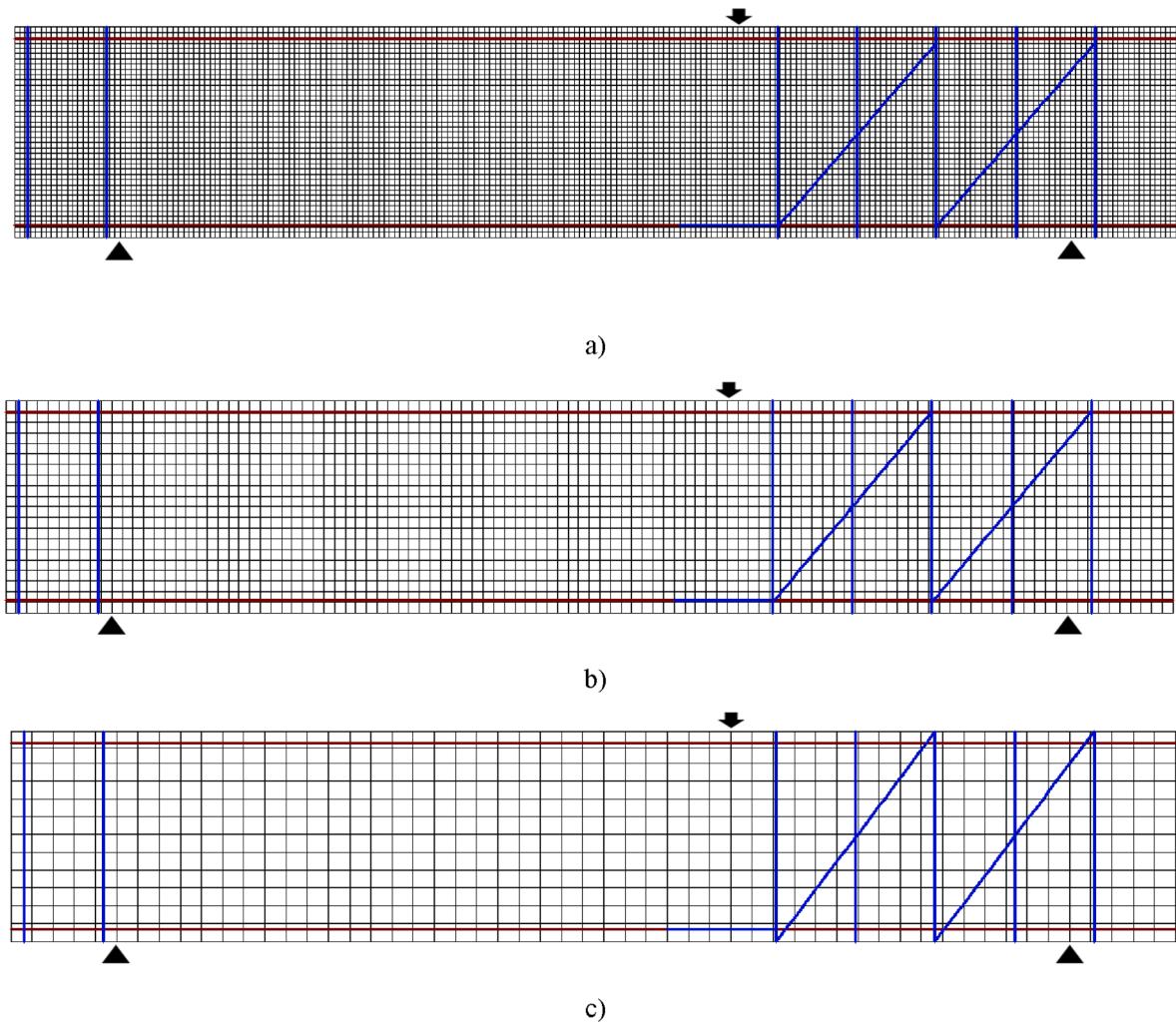


Fig. 6. Mesh refinements adopted in the numerical simulations of experimentally tested beams by using finite elements of size: (a) $10 \times 10 \text{ mm}^2$; (b) $20 \times 20 \text{ mm}^2$; and (c) $40 \times 30 \text{ mm}^2$ (width \times depth). Longitudinal reinforcement: brown lines; Transversal reinforcement: blue lines; Concrete: square mesh. (For interpretation of the references to color in this figure legend, the reader is referred to the web version of this article.)

registered experimentally and obtained numerically for the three levels of mesh refinement and assuming perfect bond conditions for the GFRP bars. It is verified that the responses are very similar, with small differences in the last stage of the simulations, with a tendency to approximate to the experimentally registered maximum load and its corresponding deflection with the increase of the mesh refinement. It is possible to conclude that the adopted MDFSCM assures mesh objectivity in terms of load–deflection response of the tested beams that failed in shear.

The crack pattern obtained numerically at the last converged loading step shows that the shear failure crack is formed by relatively high number of cracks completely open (pink color). According to the numerical model, the cracks in this stage do not have capacity of transferring between their faces any type of stress component. This corresponds to the imminent stage of the brittle failure mode of the beam, observed experimentally, which numerically corresponds to the formation of an instable mechanism (the beam is being decomposed in two parts separated by the shear failure crack), and no convergence is any more possible to assure.

Fig. 8 compares the crack patterns registered experimentally and obtained numerically for the three levels of mesh refinement. It is verified that all the adopted mesh refinements have captured a crack pattern corresponding to shear failure, but as finer is the mesh refinement, as precise, in general, is the prediction in terms of the localization

and shape of the critical shear cracks.

3.4. Performance on predicting moment–curvature and concrete strains

Taking into consideration the conclusions obtained from the analysis in the previous section, and the computing time required for the three mesh refinements, the intermediate one (finite elements of $20 \times 20 \text{ mm}^2$ dimension) was adopted in the analysis of this and next sections.

This section aims to assess the performance of the MDFSCM in predicting the measured loading vs concrete strains and the moment–curvature response of the tested beams. For the first objective, the 5 ϕ 12 and 3 ϕ 12/2 ϕ 12 beams were selected, the former one being representative of the beams of one layer and the later for the beams with two layers of flexural reinforcement. The load versus principal strain diagrams, recorded experimentally in the delta rosettes shown in Fig. 2, are compared to the numerical predictions in Fig. 9. These principal strains are obtained experimentally from the following equation:

$$\varepsilon_{1,2} = \frac{1}{3}(\varepsilon_a + \varepsilon_b + \varepsilon_c) \pm \frac{\sqrt{2}}{3} \sqrt{(\varepsilon_a - \varepsilon_b)^2 + (\varepsilon_b - \varepsilon_c)^2 + (\varepsilon_a - \varepsilon_c)^2} \quad (6)$$

where ε_a , ε_b and ε_c are the strains in each of the three components forming a delta rosette, determined from the displacements recorded by the LVDTs (by dividing the measured displacement by the base-reference length of 200 mm, Fig. 2). Only the rosette crossed by the

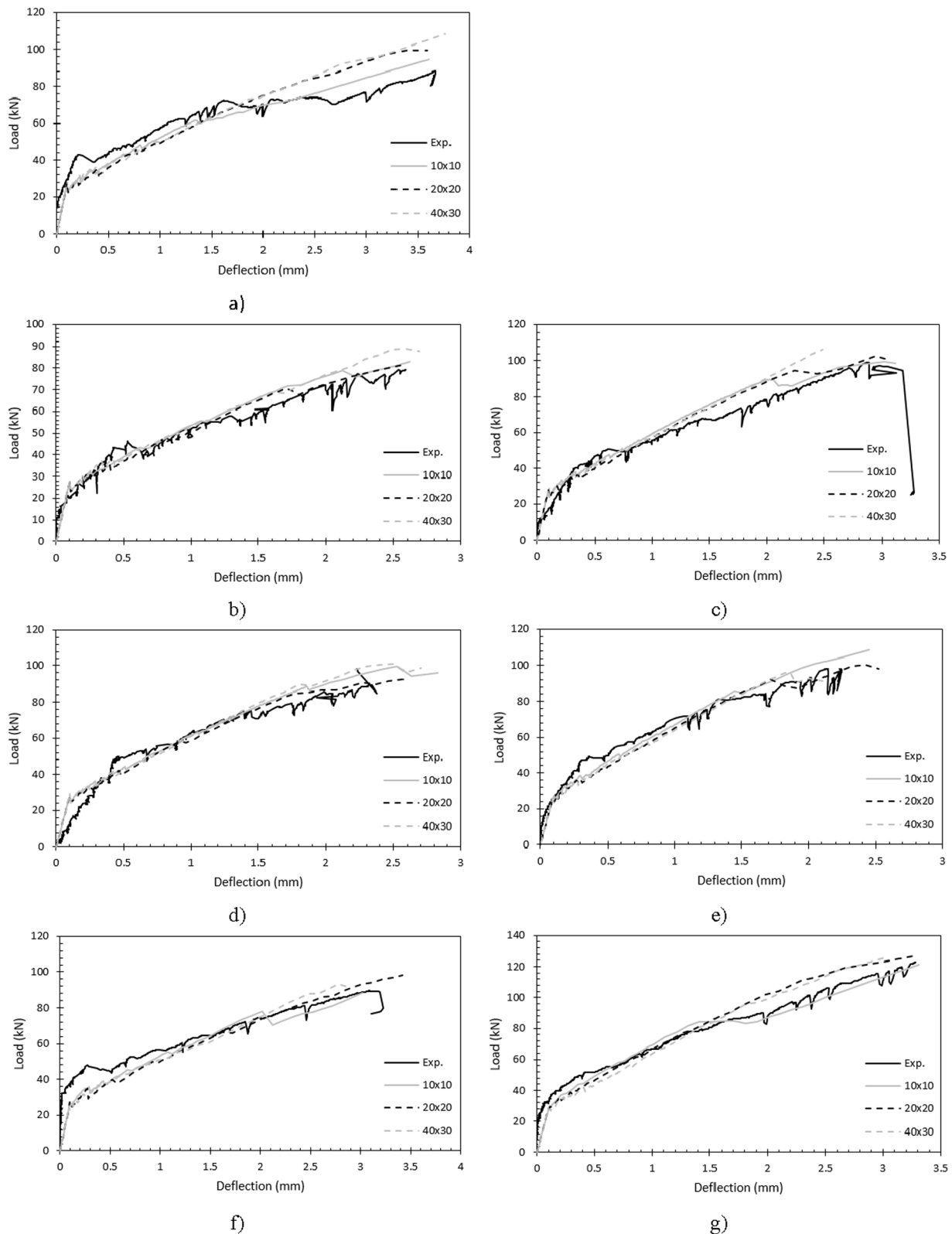


Fig. 7. Effect of mesh refinement on the force–deflection response of beams: (a) 5φ12; (b) 3φ16; (c) 3φ18; (d) 4φ16; (e) 4φ18; (f) 3φ12/2φ12; (g) 3φ18/1φ18.

shear failure crack was taken into consideration on the evaluation of the principal strains ε_1 and ε_2 in the concrete representative of this rosette.

It is verified that, despite being capable of predicting reasonably the qualitative evolution of the load vs principal strain, the numerical model has, however, the tendency of predicting larger strains. The largest differences occur at crack initiation stage, becoming the numerical

predictions closer to the experimental ones with the approximation to the beam's failure load. It should be noted that a strain measure recorded experimentally is quite dependent on the relative location between the strain sensor and the closest cracks. Therefore, it is a local measure, representing exclusively the strain in the region where this sensor is localized, being expectable a smaller predictive performance of this type

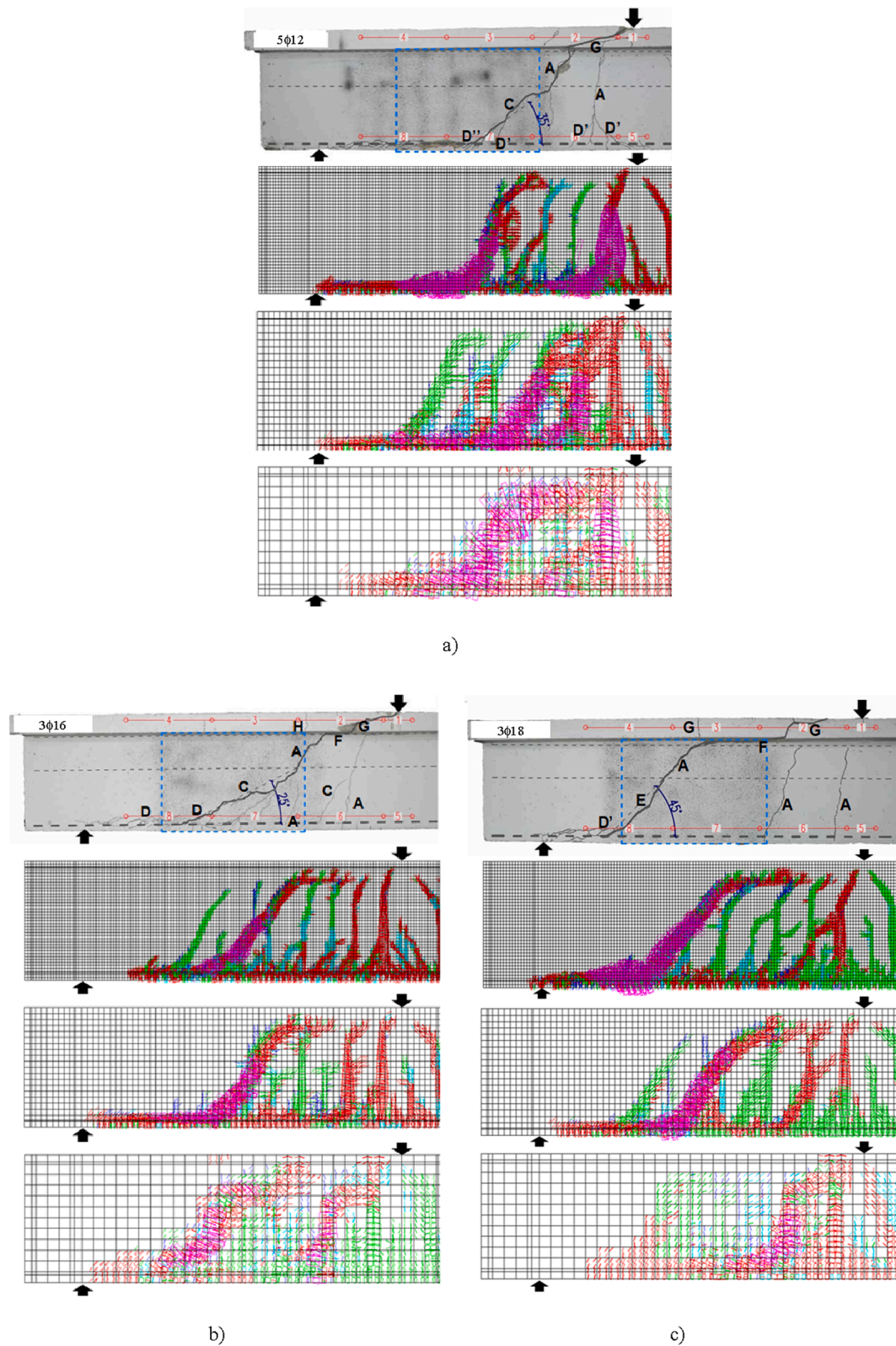


Fig. 8. Effect of mesh refinement on the crack patterns of beams: (a) 5φ12; (b) 3φ16; (c) 3φ18; (d) 4φ16; (e) 4φ18; (f) 3φ12/2φ12; (g) 3φ18/1φ18. Color representation of the crack status pink = crack completely open; red = crack in the opening process; cyan = crack in the reopening process; green = crack in the closing process; blue = closed crack. (For interpretation of the references to color in this figure legend, the reader is referred to the web version of this article.)

of information. This was a common feature to almost type of FEM-based constitutive models that have participated in the blind simulation competition of R/SFRC beams of real scale failed in shear [32].

The predictive performance of the MDFSCM was also assessed by determining the moment vs curvature ($M-\gamma$) of the 3φ18 and 3φ18/1φ18 beams, the former one being representative of the beams of one layer

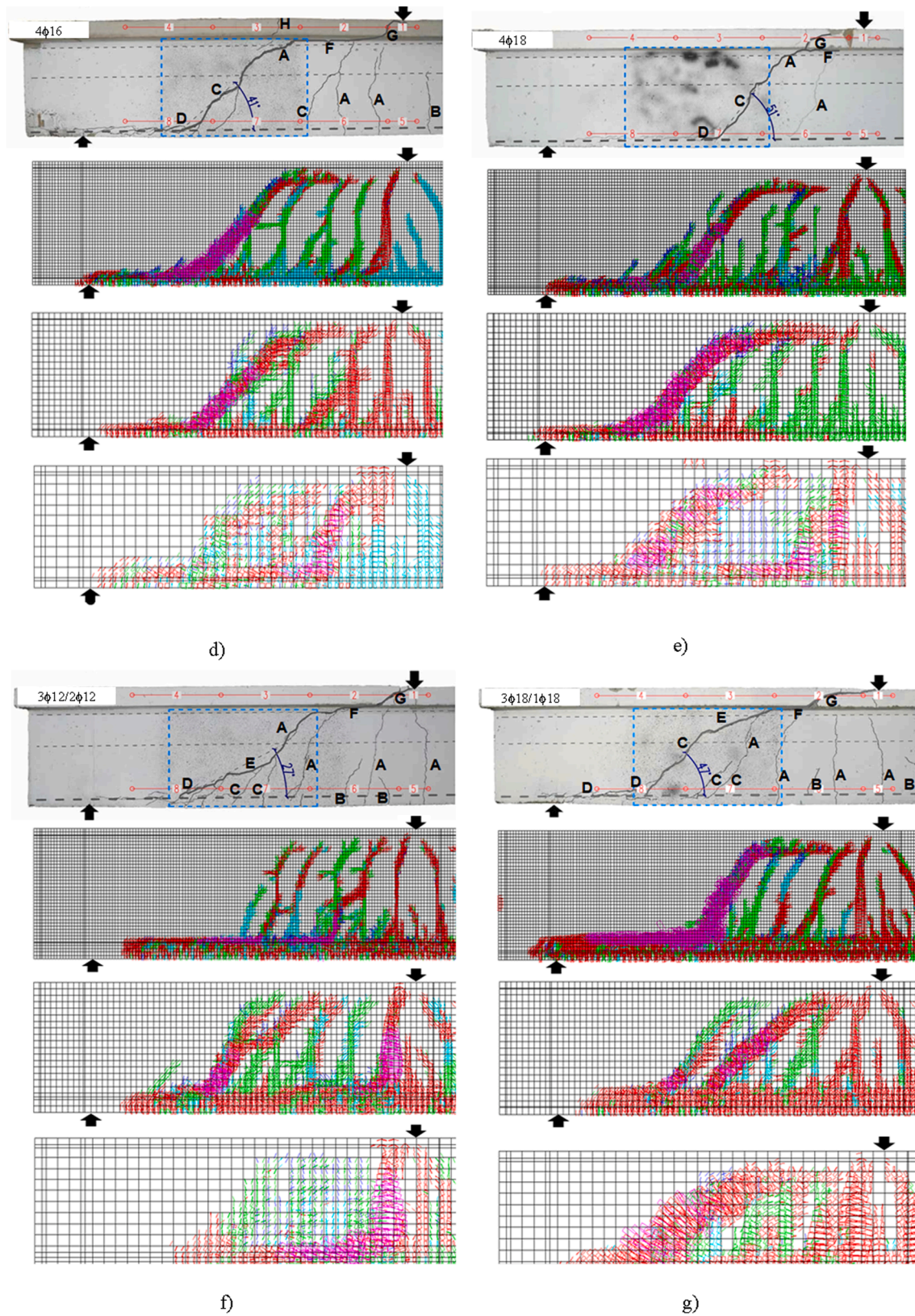


Fig. 8. (continued).

and the later for the beams with two layers of flexural reinforcement. The $M-\chi$ that is compared corresponds to the loaded section, therefore the curvature is obtained from the displacements recorded in the LVDTs 1 and 5 (the corresponding strain is determined by dividing the

displacement by the measuring reference length of the LVDT) and considering the distance between these LVDTs (Fig. 1). The evaluation of the curvature obtained numerically has followed a strategy similar to the experimental one, by considering the displacement of the nodes of the

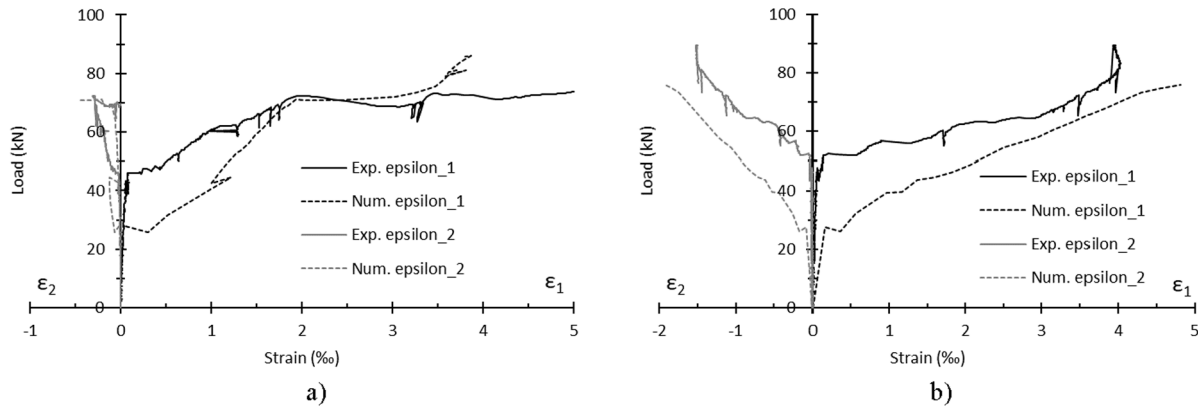


Fig. 9. Load versus principal strains obtained experimentally and numerically in the beams: (a) 5φ12; and (b) 3φ12/2φ12.

finite element mesh disposed in correspondence to that LVDTs. The bending moment was calculated at the beam's loaded section. The comparison of experimental and numerical $M-\chi$ for that beams are shown in Fig. 10, where excellent predictive performance is demonstrated for the MDFSCM in this respect.

3.5. Influence of bond conditions between flexural reinforcement and surrounding concrete

This section aims to assess how different modeling conditions for the bond between flexural reinforcement and surrounding concrete affect the relevant results of the type of beams that are being simulated. For this purpose, the 5φ12, 3φ18 and 3φ12/2φ12 beams were simulated by assuming perfect bond and considering IFE of four nodes with 2 G-Lo-IS, and adopting the constitutive law introduced in Section 3.2.3 (Eq. (4), Fig. 5) with the following values for the model parameters: $\delta_0=0.03$ mm; $\delta_m=0.5$ mm; $\tau_m=18$ MPa; $\beta_1=0.15$; $\beta_2=0.25$; $K_n=10000$ MPa/mm (stiffness in opening direction of the IFE). These values were derived from the work of Pepe et al. [53], where similar GFRP bars were used, and the local bond law was determined from inverse analysis using the results from pull-out bending tests (force versus loaded end slip and free end slip). Fig. 11 compares the force–deflection for these two types of bond conditions. In the legend of this figure, DB-IFE means that interface finite elements were disposed at the flexural reinforcement–surrounding concrete, while PB signifies that perfect bond conditions were adopted. The results show that modeling the possibility of occurring debond between the flexural reinforcement and surrounding concrete provides better simulations, mainly close to the failure of the beams. Fig. 12 shows that the crack pattern is also better predicted when using interface finite elements.

3.6. Influence of the approach for simulating the crack shear stress transfer

When using smeared crack approaches, the shear retention factor, β , is currently used to simulate the degradation of crack shear stress transfer mechanisms (Eq. (2)) by adopting a constant value or a function of the following type:

$$\beta = \left(1 - \frac{\epsilon_n^{cr}}{\epsilon_{n,u}^{cr}} \right)^{p_1} \quad (7)$$

where ϵ_n^{cr} is the actual crack normal strain, $\epsilon_{n,u}^{cr}$ is the ultimate crack normal strain (Fig. 3) and $p_1 = 3$ was adopted for ensuring a high decrease of β with the increase of ϵ_n^{cr} . In the simulations where the crack shear softening diagram was used, as described in Section 3.2.1, the values of the model parameters indicated in Table 3 were adopted. For the comparison purpose, the 5φ12 and 3φ12/2φ12 beams were simulated, but the relevant derived conclusions can be regarded representative of RC beams failing in shear. The obtained force–deflection relationship and the crack patterns are shown in Figs. 13 and 14, respectively.

By using the shear retention factor for simulating the crack shear stress transfer, the load carrying capacity of the simulated beams was overestimated (Fig. 13), and the shear failure crack was not identified in the crack pattern (Fig. 14). When adopting the crack shear softening diagram, a much better prediction of the maximum load and corresponding deflection was obtained (Fig. 13), with clear identification of the shear failure cracks in the obtained crack patterns (Fig. 14).

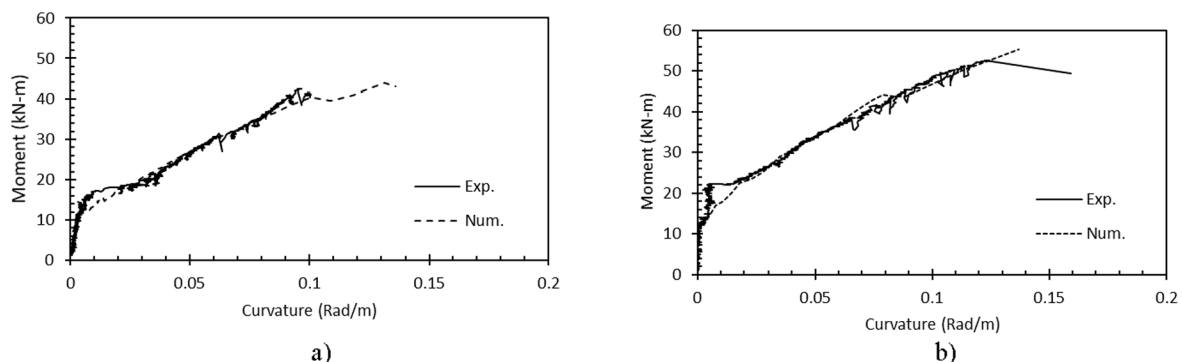


Fig. 10. Experimental vs numerical simulations of the moment–curvature relationship in the beams: (a) 3φ18; and (b) 3φ18/1φ18.

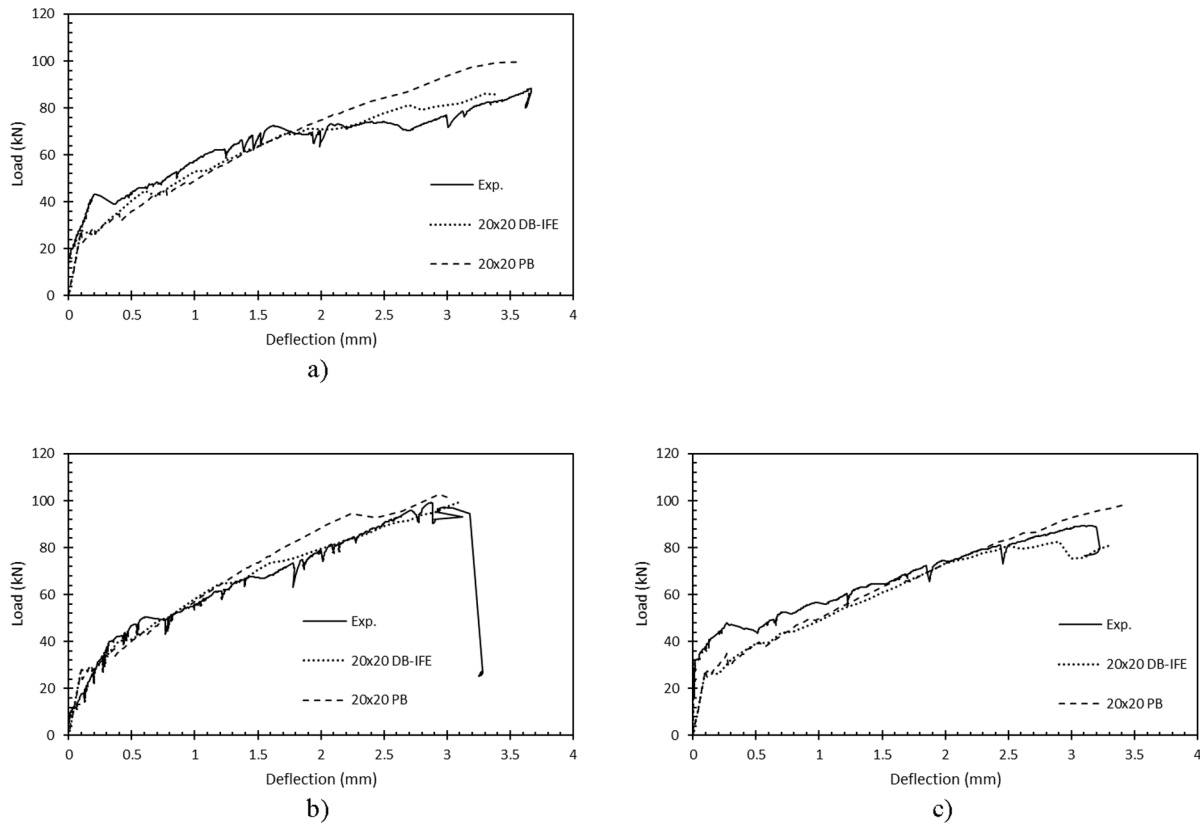


Fig. 11. Effect of bond conditions on the force–deflection response of beams: (a) 5φ12; (b) 3φ18; (c) 3φ12/2φ12 (DB-IFE: Debond simulated with interface FE; PB: Perfect Bond).

3.7. Parametric study for assessing the influence of the parameters defining the crack shear softening diagram on the model's predictive performance

For obtaining the crack shear softening diagram represented in Fig. 4, experimental direct shear tests, complemented with inverse analysis, is a strategy that is being attempted [54]. However, assuring pure shear conditions in experimental tests is quite challenging [55–58], since fracture mix modes are always present in the critical regions [59–61], therefore the reliability of the results obtained from this strategy is arguable. In consequence, it is opportune to figure out the influence of each parameter of the crack shear softening diagram on the predictive performance of the MDFSCM, namely the β parameter that, together with the τ_{tp}^{cr} , define the stiffness of the pre-peak branch (see Fig. 4), as well as the $G_{F,II}$ that, together with the τ_{tp}^{cr} , determine the softening branch. For this purpose, the 4φ16 beam was selected for this parametric study, but the relevant derived conclusions can be regarded representative of RC beams failing in shear. To assess the influence of each one of these parameters, the values of the entire model parameters remained the same except those corresponding to the parameter to be investigated.

Fig. 15 shows the influence of the β parameter on the force–deflection response of the 4φ16 beam. It is verified that the simulations start having differences only when critical shear cracks start becoming localized (close to the deflection of 1.5 mm), as shown in Fig. 16, where the crack patterns for deflection at 1.5 mm and at failure are represented (for the simulation with $\beta = 0.1$, the ultimate crack pattern corresponds to the deflection of 3 mm). At that stage, the load carrying capacity of the beam decreases with the increase of the value of the β parameter. The simulations with $\beta = 0.1$ provided more diffuse crack patterns, leading to a higher consume of fracture energy, and, consequently, to a higher load carrying capacity above that deflection level. According to

Eq. (2), $D_{t,1}^{cr}$ increases with β , and since τ_{tp}^{cr} is maintained constant in the simulations, the entrance in the crack shear softening stage is anticipated for higher values of β , therefore crack shear damage is intensified and the critical shear crack is localized.

Fig. 17 shows the influence of the τ_{tp}^{cr} parameter on the force–deflection response of the 4φ16 beam. It is verified that the load carrying capacity increases with τ_{tp}^{cr} . For the smallest value, shear failure localization has been anticipated due to the entrance of the critical shear cracks in their softening stage. For the largest value of τ_{tp}^{cr} , shear failure localization is postponed for larger deflection level, and can even not occur in case of beams with relatively low reinforcing ratio of steel bars due to flexural failure occurrence (in the present case this does not happen due to the linear-brittle failure nature of the GFRP bars).

Finally the influence of the $G_{F,II}$ on the force–deflection response of the 4φ16 beam is shown in Fig. 18. It is verified, from the quality point of view, that $G_{F,II}$ has an influence similar to the τ_{tp}^{cr} , and the value of better predictive performance is almost half of the $G_{F,I}$.

4. Conclusions

This work has assessed the potentialities and debilities of a multi-directional fixed smeared crack model (MDFSCM) for simulating the behavior of reinforced concrete beams failing in shear. Seven experimentally tested beams reinforced with longitudinal GFRP bars were numerically simulated. Based on the results from the simulations, the following conclusions can be pointed out:

1. MDFSCM similar to the adopted one is able of predicting the relevant behavioural features of beams failing in shear if a shear softening law is adopted for modeling the crack shear stress transfer, and proper values are adopted for the model parameters;

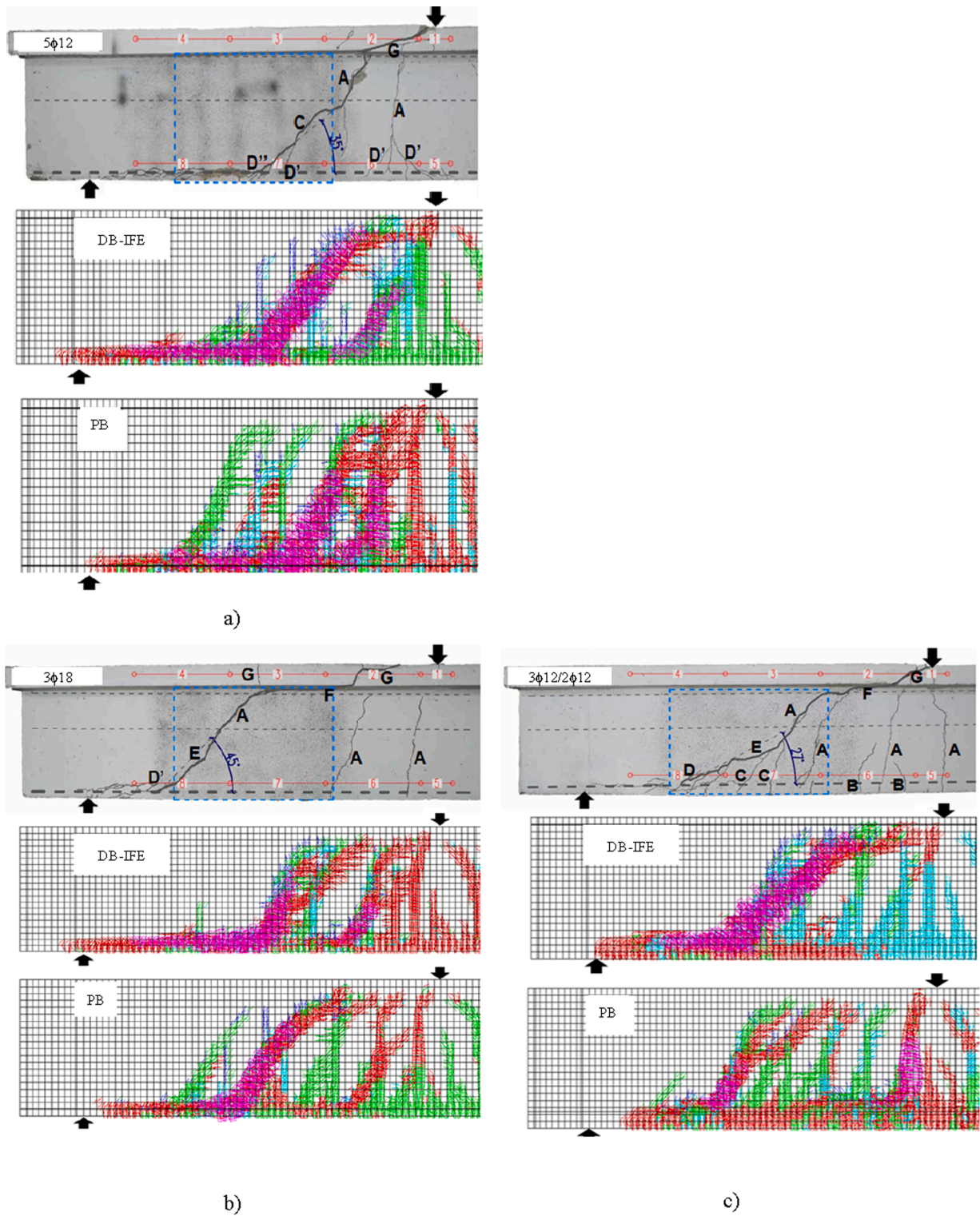


Fig. 12. Effect of bond conditions on the crack patterns of beams: (a) 5 ϕ 12; (b) 3 ϕ 18; (c) 3 ϕ 12/2 ϕ 12 (DB-IFE: Debond simulated with interface FE; PB: Perfect Bond). Color representation of the crack status pink = crack completely open; red = crack in the opening process; cyan = crack in the reopening process; green = crack in the closing process; blue = closed crack. (For interpretation of the references to color in this figure legend, the reader is referred to the web version of this article.)

2. By using mesh refinements composed by finite elements of maximum edge size up to 5 times the maximum aggregate size (D_{max}), the relevant results were marginally affected by the finite element mesh refinement, namely the force–deflection and the crack pattern. A clear shear failure was captured for all the adopted mesh refinements when using a softening diagram for modeling the crack shear stress

transfer. However, by refining the finite element mesh up to finite elements of edge size of $1.25D_{max}$, more realistic crack patterns were captured;

3. MDFSCM has predicted with high accuracy the moment curvature ($M-\gamma$), but a tendency for predicting larger strains was obtained, mainly at initial stage of crack propagation;

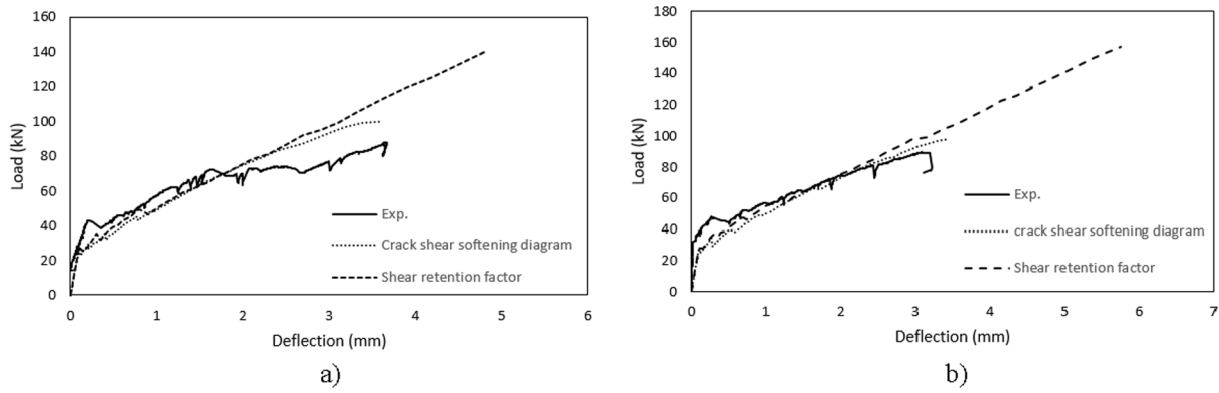


Fig. 13. Influence of the crack shear approach on the load–deflection response in the beams: (a) 5φ12; and (b) 3φ12/2φ12.

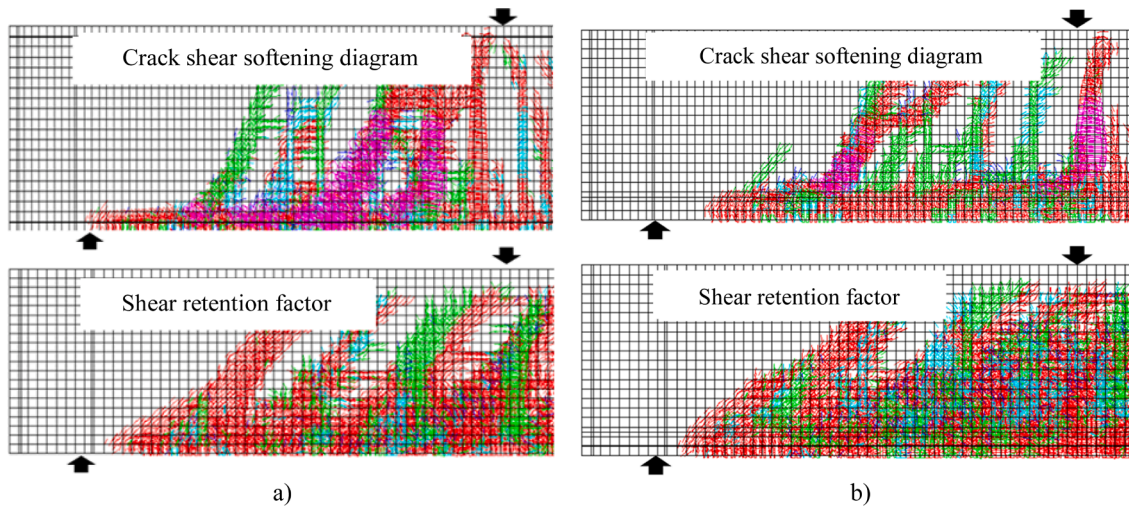


Fig. 14. Influence of the crack shear approach on the crack patterns of the beams: (a) 5φ12; and (b) 3φ12/2φ12. Color representation of the crack status pink = crack completely open; red = crack in the opening process; cyan = crack in the reopening process; green = crack in the closing process; blue = closed crack. (For interpretation of the references to color in this figure legend, the reader is referred to the web version of this article.)

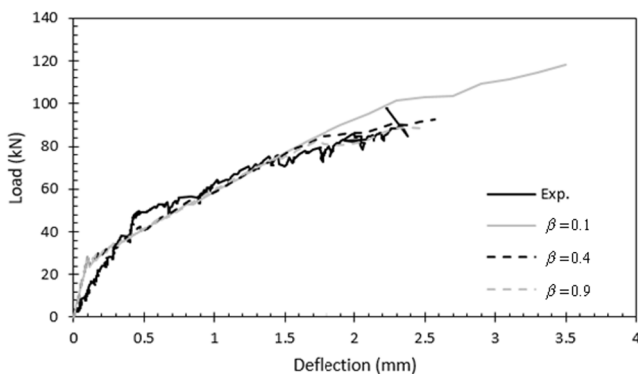


Fig. 15. Influence of the β parameter of the crack shear softening diagram on the load–deflection response of 4φ16 beam.

4. The use of interface finite elements, with a local bond law representative of real bond conditions between GFRP and surrounding concrete, has provided better simulations, mainly close to the failure of the beams, as well as more realistic crack patterns;
5. The use of the shear retention factor concept for simulating the crack shear stress transfer has overestimated the load carrying capacity and a crack pattern corresponding to a shear failure was not formed. When adopting the crack shear softening diagram, a much better

prediction of the maximum load and corresponding deflection was obtained, with crack patterns identifying the occurrence of a shear failure;

6. The behavior of the crack shear softening diagram is influenced by the parameters that define the model. It is verified that the load carrying capacity increases with the crack shear strength, τ_{tp}^c . For the largest adopted value of τ_{tp}^c ($\tau_{tp}^c = 2.0 \text{ MPa}$), shear failure localization is postponed to a larger deflection level. Similar conclusion can be made considering the influence of the mode II fracture energy, $G_{F,II}$ ($G_{F,II} = 0.09 \text{ N/mm}$). The β parameter, together with the τ_{tp}^c , define the stiffness of the pre-peak branch of this diagram. It was verified that the load carrying capacity of the beam has decreased with the increase of the value of the β parameter (from 0.1 to 0.9), since the entrance in the crack shear softening stage is anticipated for higher values of β , promoting the shear failure localization. However, specific research must be conducted on reliable experimental methodologies for assessing the values of the parameters defining the softening diagram simulating the crack shear stress transfer.

CRedit authorship contribution statement

Joaquim A.O. Barros: Conceptualization, Methodology, Resources, Investigation, Validation, Formal analysis, Data curation, Supervision, Writing - original draft, Visualization, Project administration, Funding acquisition. **Hadi Baghi:** Methodology, Formal analysis, Investigation,

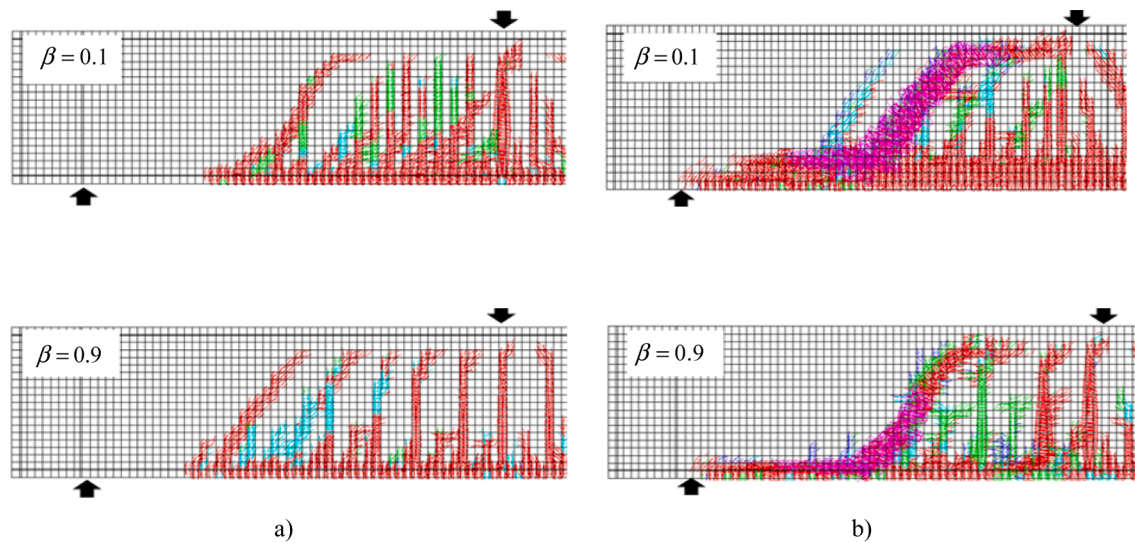


Fig. 16. Influence of the β parameter of the crack shear softening diagram on the crack pattern of 4 ϕ 16 beam at the deflection of a) 1.5 mm; b) ultimate deflection (3 mm in case of $\beta = 0.1$). Color representation of the crack status pink = crack completely open; red = crack in the opening process; cyan = crack in the reopening process; green = crack in the closing process; blue = closed crack. (For interpretation of the references to color in this figure legend, the reader is referred to the web version of this article.)

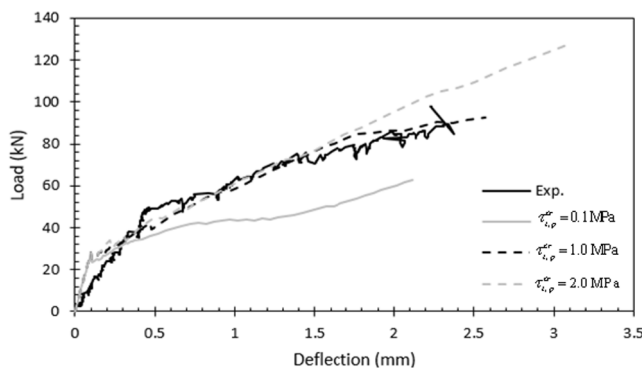


Fig. 17. Influence of the $\tau_{c,p}^{cr}$ parameter of the crack shear softening diagram on the load–deflection response of 4 ϕ 16 beam.

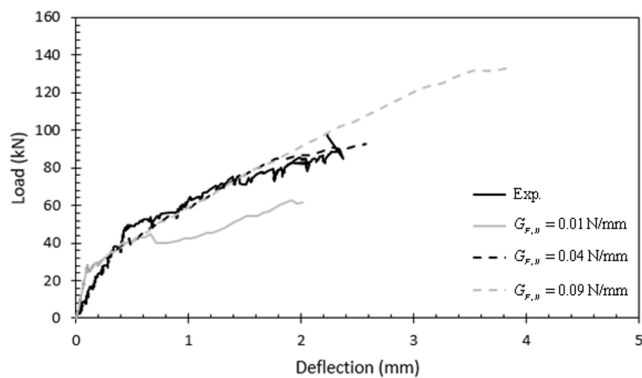


Fig. 18. Influence of the $G_{F,II}$ parameter of the crack shear softening diagram on the load–deflection response of 4 ϕ 16 beam.

Data curation, Writing - review & editing. **A. Ventura-Gouveia:** Formal analysis, Investigation, Data curation, Writing - review & editing.

Declaration of Competing Interest

The authors declare that they have no known competing financial

interests or personal relationships that could have appeared to influence the work reported in this paper.

Acknowledgements

The first author aims to acknowledge the support provided by FCT through the research project ICOSyTec -Innovative construction system for a new generation of high performance buildings, with reference: POCI-01-0145-FEDER-027990.

References

- [1] Ahmed EA, Benmokrane B, Sansfaçon M. Case study: design, construction, and performance of the La Chancelière parking Garage's concrete flat slabs reinforced with GFRP bars. *J Compos Constr* 2017;21(1):05016001.
- [2] Manalo A, Benmokrane B, Park K-T, Lutz D. Recent developments on FRP bars as internal reinforcement in concrete structures. *Concr Australia* 2014;40(2):46–56.
- [3] Mazaheripour H, Barros JAO, Soltanzadeh F, Sena-Cruz J. Deflection and cracking behavior of SFRSCC beams reinforced with hybrid prestressed GFRP and steel reinforcements. *Eng Struct* 2016;125:546–65.
- [4] Soltanzadeh F, Edalat-Behbahani A, Barros JAO, Mazaheripour H. Effect of fiber dosage and prestress level on shear behavior of hybrid GFRP-steel reinforced concrete I-shape beams without stirrups. *Compos B Eng* 2016;102:57–77. <https://doi.org/10.1016/j.compositesb.2016.07.003>.
- [5] Barris C, Torres LI, Turon A, Baena M, Catalan A. An experimental study of the flexural behaviour of GFRP RC beams and comparison with prediction models. *Compos Struct* 2009;91(3):286–95.
- [6] Benmokrane B, El-Salakawy E, El-Ragaby A, Lackey T. Designing and testing of concrete bridge decks reinforced with glass FRP bars. *J Bridge Eng* 2006;11(2):217–29.
- [7] Canadian Standards Association (CSA 2002). Design and construction of building components with fibre reinforced polymers. CAN/CSA S806-02, Rexdale, Ontario, Canada.
- [8] ACI Committee 440. Guide for the design and construction of concrete reinforced with FRP bars (ACI 440.1R-06). American Concrete Institute, Farmington Hills, MI, USA; 2001.
- [9] fib bulletin 40 (2007). FRP reinforcement in RC structures, Technical Report, 160 pages, ISBN: 978-2-88394-080-2.
- [10] Yan F, Lin Z, Yang M. Bond mechanism and bond strength of GFRP bars to concrete: a review. *Compos B Eng* 2016;98:56–69.
- [11] Rosa IC, Firmo JP, Correia JR, Barros JAO. Bond behaviour of sand coated GFRP bars to concrete at elevated temperature – Definition of bond vs. slip relations. *Compos B Eng* 2019;160:329–40.
- [12] Solyom S, Di Benedetto M, Guadagnini M, Balázs GL. Effect of temperature on the bond behaviour of GFRP bars in concrete. *Compos B Eng* 2020;183:10. <https://doi.org/10.1016/j.compositesb.2019.107602>.
- [13] Escórcio PCC. Experimental and analytical study of concrete structures reinforced with GFRP bars, PhD Thesis, University of Madeira, Funchal, Portugal; 2016.

- [14] Yost JR, Gross SP, Dinehart DW. Shear strength of normal strength concrete beams reinforced with deformed GFRP bars. *J Compos Constr* 2001;5(4):268–75. [https://doi.org/10.1061/\(ASCE\)1090-0268\(2001\)5:4\(268\)](https://doi.org/10.1061/(ASCE)1090-0268(2001)5:4(268)).
- [15] Al-Khrdaji T, Wideman M, Belarbi A, Nanni A. Shear strength of GFRP RC beams and slabs. In: *Proceedings of the International Conference on Composites in Construction – CCC 2001*, Porto, Portugal, Oct. 10–12, J Figueiras, L. Juvandes and R. Fúria, Eds., 2001;1:409–414.
- [16] El-Sayed AK, El-Salakawy EF, Benmokrane B. Shear capacity of high-strength concrete beams reinforced with fiber-reinforced polymer bars. *ACI Struct J* 2006; 103(3):383–9. <https://doi.org/10.14359/15316>.
- [17] El-Sayed AK, El-Salakawy EF, Benmokrane B. Shear strength of fibre-reinforced polymer reinforced concrete deep beams without web reinforcement. *Can J Civ Eng* 2012;39(5):546–55.
- [18] Matta F, El-Sayed AK, Nanni A, Benmokrane B. Size effect on concrete shear strength in beams reinforced with fiber-reinforced polymer bars. *ACI Struct J* 2013; 110(4):617–28.
- [19] Tureyen AK, Frosch RJ. Shear tests of FRP-reinforced concrete beams without stirrups. *ACI Struct J* 2002;99(4):427–34. <https://doi.org/10.14359/12111>.
- [20] Razaqpur AG, Isgor BO, Greenaway S, Selley A. Concrete contribution to the shear resistance of fiber reinforced polymer reinforced concrete members. *J Compos Constr* 2004;8(5):452–60.
- [21] Kaszubska M. Analysis of the flexural reinforcement on shear capacity of concrete beams without transversal reinforcement. PhD thesis. Lodz University of Technology (in Polish); 2018.
- [22] Kaszubska M, Kotynia R, Barros JAO, Baghi H. Shear behavior of concrete beams reinforced exclusively with longitudinal glass fiber reinforced polymer bars: experimental research. *Struct Concr* 2018;19:152–61. <https://doi.org/10.1002/suco.201700174>.
- [23] Cervera M, Chiumenti M. Smeared crack approach: back to the original track. *Int J Numer Anal Meth Geomech* 2006;30(12):1173–99.
- [24] Rodrigues EA, Manzoli OL, Bitencourt Jr. LAG, Bittencourt TN. 2D meso- scale model for concrete based on the use of interface element with a high aspect ratio. *Int J Solids Struct* 94–95, 112–124, ISSN 00207683; 2016. doi: 10.1016/j.jisolsr.2016.05.004.
- [25] Simone A. Partition of unity-based discontinuous finite elements: GFEM, PUFEM, XFEM. *Revue Européenne de Génie Civil*, 11(7–8), 1045–1068, ISSN 1774-7120; 2007. doi: 10.1080/17747120.2007.9692976.
- [26] Jirásek M, Zimmermann T. Embedded crack model. Part I: basic formulation. *Int J Num Methods Eng* 2001;50(6):1269–90. [https://doi.org/10.1002/1097-0207\(20010228\)50:6<1269::AID-NME11>3.0.CO;2-U](https://doi.org/10.1002/1097-0207(20010228)50:6<1269::AID-NME11>3.0.CO;2-U).
- [27] Jirásek M, Zimmermann T. Embedded crack model. Part II: combination with smeared cracks. *Int J Numer Meth Eng* 2001;50(6):1291–305. [https://doi.org/10.1002/1097-0207\(20010228\)50:6<1291::AID-NME12>3.0.CO;2-Q](https://doi.org/10.1002/1097-0207(20010228)50:6<1291::AID-NME12>3.0.CO;2-Q).
- [28] Dias-da-Costa D. Strong Discontinuities in the scope of the Discrete Crack Approach. PhD Thesis, Civil Engineering Department, University of Coimbra, Coimbra, Portugal; 2010.
- [29] Schlangen E., van Mier J. Experimental and numerical analysis of micromechanisms of fracture of cement-based composites. *Cem Concr Compos* 1992;14(2):105–118, ISSN 0958-9465, doi: 10.1016/0958-9465(92)90004-F.
- [30] Baghi H, Barros JAO, Rezazadeh M. Shear strengthening of damaged reinforced concrete beams with Hybrid Composite Plates. *Compos Struct* 2017;178:353–71.
- [31] fib bulletin 45, 2018. Practitioner's guide to finite element modelling of reinforced concrete structures. State-of-art report prepared by Task Group 4.4, ISBN 978-88394-085-7, Sprint-Digital-Druck.
- [32] Barros J.A.O., Merino B.S. (2020). Retrieved from <https://www.fib-international.org/blog/412-blind-competition-on-numerical-stimulation-of-frc-beams-results.html>.
- [33] Fehling E., Bullo T., 2002. Ultimate load capacity of reinforced Steel fibre concrete deep beams subjected to shear. *Finite Elements in Civil Engineering Applications: Proceedings of the Third Diana World Conference*, Tokyo, Japan, 9–11 October, M. A.N. Hendriks, J.A. Rots Eds., 209–218.
- [34] Rots JG, Nauta P, Kusters GMA, Blaauwendraad J. Smeared crack approach and fracture localization in concrete. *HERON* 1985;30(1):1–48.
- [35] Rots JG. Computational modeling of concrete fracture. PhD Thesis. Delft University of Technology; 1988.
- [36] Huber P, Kollegger J. Numerical simulation of shear behavior of reinforced concrete beams with and without flanges. *Computational Modelling of Concrete Structures*, Proceedings of the EURO-C 2014, St. Anton Am Arlberg, Austria, 24–27 March, Volume I, Nenad Bicanic, Herbert Mang, Gunther Meschke, René de Borst Eds; 2014:1073–1080.
- [37] Puijssers AF. Description of the stiffness relation or mixed-mode fracture problems in concrete using the rough-crack model of Walraven, TU-Delft Report, Department of Civil Engineering, No. 5-28-2; 1985.
- [38] Cervenka V., Pukl H., Eligehausen R., 1990. Computer simulation of anchoring technique and design of concrete structures, *Proc. Second Intern. Conf. on Computer Aided Analysis and Design of Concrete Structures*, Zell am See, Austria, pp. 1–19.
- [39] Sena-Cruz JM. Strengthening of concrete structures with near-surface mounted CFRP laminate strips. PhD Thesis. University of Minho, Guimarães, Portugal; 2004.
- [40] Ventura-Gouveia A. Constitutive models for the material nonlinear analysis of concrete structures including time-dependent effects. PhD Thesis. University of Minho, Guimarães, Portugal; 2011.
- [41] Breveglieri M, Barros JAO, Aprile A, Ventura-Gouveia A. Strategies for numerical modeling the behavior of RC beams strengthened in shear using the ETS technique. *Eng Struct* 2016;128:296–315.
- [42] Rots JG, de Borst R. Analysis of mixed-mode fracture in concrete. *J Eng Mech ASCE* 1987;113(11):1739–58.
- [43] Teixeira MDE, Barros JAO, Cunha VMCF, Moraes-Neto BN, Ventura-Gouveia A. Numerical simulation of the punching shear behaviour of self-compacting fibre reinforced flat slabs. *Const Build Mater J*, 74, 25–36.
- [44] Sena-Cruz JM, Barros JAO, Azevedo AFM, Ventura-Gouveia A. Numerical simulation of the nonlinear behavior of RC beams strengthened with NSM CFRP strips. In: *Proceedings of CMNE/CILAMCE Congress*, FEUP, Porto, Portugal, 13–15 June; 2007.
- [45] ISO 10406-1:2015(E). Fibre-reinforced polymer (FRP) reinforcement of concrete. Test methods - Part 1: FRP bars and grids.
- [46] EN 206-1:2000 Concrete - Part 1: Specification, performance, production and conformity.
- [47] Edalat Behbahani A, Barros JAO, Ventura-Gouveia A. Plastic-damage smeared crack model to simulate the behaviour of structures made by cement based materials. *Int J Solids Struct* 2015;73-74:20–40.
- [48] Cornelissen HAW, Hordijk DA, Reinhardt HW. Experimental determination of crack softening characteristics of normalweight and lightweight concrete. *HERON* 1986;31(2):45–56.
- [49] fib Model Code 2010, 2013. fib-federation internationale du beton, fib Model Code for Concrete Structures 2010. John Wiley & Sons Ltd. <https://doi.org/10.1002/9783433604090>.
- [50] RILEM. Draft Recommendation, 50-FMC Committee Fracture Mechanics of Concrete. Determination of the fracture energy of mortar and concrete by means of three-point bending tests on notched beams. *Materials and Structures*, 18, N° 106; 1985:285–290.
- [51] Barros JAO, Baghi H, Dias SJE, Ventura-Gouveia A. A FEM-based model to predict the behaviour of RC beams shear strengthened according to the NSM technique. *Eng Struct* 2013;56:1192–206.
- [52] Barros J.A.O., 1995. Comportamento do betão reforçado com fibras – análise experimental e simulação numérica (Behavior of FRC – experimental analysis and numerical simulation). PhD Thesis, Civil Eng. Dept., Faculty of Engineering, University of Porto, Portugal [in Portuguese].
- [53] Pepe M, Mazaheripour H, Barros JAO, Sena-Cruz JM, Martinelli E. Numerical calibration of bond laws for GFRP bars embedded in steel fiber-reinforced self-compacting concrete. *Compos B Eng* 2013;50:403–12.
- [54] Baghi H, Barros JAO. Shear properties of the strain hardening cementitious composite material. *J Mater Civ Eng* 2016;28(10):04016093.
- [55] Soltanzadeh, Barros JAO, Santos RFC (2015). High performance fiber reinforced concrete for the shear reinforcement: experimental and numerical research. *Constr Build Mater J* F;77: 94–109.
- [56] Reinhardt HW, Osbolt J, Xu S, Dinku A. Shear of structural concrete members and pure mode II testing. *Adv Cem Based Mater* 1997;5(3):75–85.
- [57] Soetens T, Matthys S. Shear-stress transfer across a crack in steel fibre-reinforced concrete. *Cement and Concrete Composites* 2017;82:1–13.
- [58] Barragán B, Gettu R, Agulló L, Zerbino R. Shear failure of steel fibre-reinforced concrete-based push off tests. *Concrete Beton Journal* 2008;118:8–14.
- [59] Divakar MP, Fafitis A, Shah SP. Constitutive model for shear transfer in cracked concrete. *J Struct Eng* 1987;113(5):1046–62.
- [60] Nooru, M.B.-Mohamed. Mixed-mode fracture of concrete: an experimental approach. PhD Thesis. Delft University of Technology; 1992.
- [61] Matos LMP, Barros JAO, Ventura-Gouveia A, Calçada RAB. Constitutive model for fibre reinforced concrete by coupling the fibre and aggregate interlock resisting mechanisms. *Cem Concr Compos* 2020;111:103618. <https://doi.org/10.1016/j.cemconcomp.2020.103618>.